ORIGINAL PAPER

Automating the repair of potholes using machine techniques and digitally crafted asphalt cartridges

Frank K. A. Awuah[1] · Alvaro Garcia-Hernandez[2] · Nick Thom[1]

© The Author(s) 2024

Abstract

Potholes are a major problem on road networks as they reduce driving safety and pavement structural integrity. Current repair methods through filling are labour-intensive and unsafe to workers. This paper presents a new approach to filling potholes with less human intervention. The proposed method adopted a modified 3D printer as the automated pothole filling machine. The machine's operational paramaters, such as extrusion speed, were optimised to maximise the extrusion rate of asphalt mixtures and enhance the efficiency of the filling process. A new digital design method was developed to quickly select the right aggregate-bitumen proportions for asphalt repair cartridges that meet desired performance standards such as extrusion rate, Marshall stability, Marshall flow, and air void contents. The quality of filled potholes was assessed by measuring the rutting depth. The machine fills exhibited 86% rutting resistance compared to hand fills, indicating its future potential to replace current manual methods.

Keywords 3D printing · Asphalt · Optimisation · Extrusion · Pothole · Automation

1 Introduction

An asphalt mixture is a composite material that is commonly used to pave roads, parking lots, and airports. It is primarily made up of mineral aggregate and a sticky substance called bitumen. The aggregates form a solid skeleton that mainly provides the required compressive strength for traffic loading, while the bitumen holds the aggregates together. As such, the proportions of aggregate and bitumen content in asphalt mixtures are carefully selected to achieve desired performance standards, such as stability under traffic loading.

A recurring irregularity in asphalt concrete is the emergence of potholes, stemming from moisture intrusion, freeze–thaw cycles, and traffic-induced loads. Moisture infiltrates cracks, expanding upon freezing and contracting during thawing, thereby weakening the asphalt. Traffic intensifies this deterioration over time, culminating in depressions. Inadequate construction, drainage, or aging worsens this phenomenon (Mchale et al. 2016; Katsamenis et al. 2023).

Within modern transportation infrastructure, the persistent challenge of potholes continues to present formidable obstacles to both road safety and maintenance (Mchale et al. 2016). These widespread disruptions not only compromise vehicle integrity and jeopardise the well-being of drivers and pedestrians but also impose substantial economic burdens on governments and societies at large. Recent data from the RAC (RAC 2023) indicates a notable increase in vehicle breakdowns attributed to potholes, with more than 8,100 incidents reported between April and June 2023, marking the highest figure in 5 years. Adding to the problem, councils have disbursed approximately £11 million in compensation to drivers for damage caused by potholes over the past 4 years.

In the last decade, there has been a significant shift towards using automation in civil engineering for sustainable construction and maintenance (Manuel Davila Delgado and

✉ Frank K. A. Awuah
  frank.awuah1@nottingham.ac.uk

  Alvaro Garcia-Hernandez
  alvaro@isac.rwth-aachen.de

  Nick Thom
  nicholas.thom@nottingham.ac.uk

1 Nottingham Transportation Engineering Centre, Department of Civil Engineering, University of Nottingham, Nottingham NG7 2RD, UK

2 ISAC, Institute of Highway Engineering, RWTH Aachen University, 2130 Bauingenieurwesen, Mies-Van-Der-Rohe-Str. 1, 52074 Aachen, Germany

Oyedele 2022; Xiao et al. 2022). Automated road repairs, for instance, promises continuous operation, safety improvements, consistent quality, reduced waste, cost savings, and integration with smart infrastructure, distinguishing it from traditional methods (Karelina et al. 2022; Eskandari Torbaghan et al. 2019). In response, industrial growth is leaning towards reducing human intervention in road pothole repair. Advanced machines such as those cited in references (JCB 2023; Velocity and Patching 2023) utilising spray injection techniques (SIT) (Kwon et al. 2018), have emerged in the past decade. However, like the throw-and-go method, SITs simultaneously blow bitumen emulsion and aggregates into potholes (Wang et al. 2022), a technique generally characterised by its lower durability and predominance in temporary or emergency repairs (Ipavec 2012).

While hot-mix asphalt offers better durability and bonding with existing pavement, regulating its temperature is a substantial challenge that affects its extrudability and lifespan, presenting a significant obstacle for pothole repair machines (Mchale et al. 2016; Ipavec 2012). Typically, flowable or pumpable mixtures are commonly linked to reduced durability (Changra and Singh 2023; Gul et al. 2022). Additionally, these 'autonomous' machines still demand significant human intervention due to technological constraints and knowledge gaps, relying on manually designed asphalt formulations. Bridging this gap poses an ongoing scientific challenge, but technologies like digital fabrication and automation hold promise for advancing intelligent pothole repairs (Davila Delgado et al. 2019; García de Soto et al. 2018; Tuvayanond and Prasittisopin 2023; Mammen and Gerling 2016). In a prior study, (Bruno et al. 2023) introduced a photogrammetry technique with the potential to predict the shape and volume of potholes. Moreover, recent advancements in automation and digital fabrication, particularly in the utilisation of 3D printing and automated machinery for hot bitumen crack filling, indicate promising prospects for automating pothole repairs (Awuah and Garcia-Hernández 2022; Gong et al. 2023). Nonetheless, a significant gap in the field of autonomous applications is the absence of knowledge concerning digitally crafted asphalt mixtures that can be extruded by autonomous machines to meet standardised volumetric and mechanical performance requirements.

Multiple factors, such as aggregate shapes, aggregate gradation, bitumen types, and bitumen content, affect how asphalt performs in the field when under traffic loading and exposed to climate and weather conditions. Existing design methods, like the Marshall Mix Design, determine aggregate gradation and binder content through a set of performance criteria like Marshall Stability and Marshall flow, which inform the designer how well the asphalt could resist deformations when pressure is applied. However, this design process is trial-and-error, labour-intensive, and takes a lot of time and resources. To optimise design and reduce manual complexity, computational methods are gaining popularity in the field (Salemi and Wang 2018; Zhang et al. 2016; Liu et al. 2018). While the Discrete Element Method (DEM) is a common technique, it demands significant computational resources (Rackl and Hanley 2017; O'Sullivan and Bray 2004; Yao et al. 2022). An innovative approach by Garcia-Hernandez et al. (Garcia-Hernandez et al. 2021a, 2021b, 2021c) utilises a Physics Engine (PE) with an impulse-based methodology to address DEM's limitations. Although PE enables real-time simulations at the cost of precision (Garcia-Hernandez et al. 2021c), it speeds up computations using predefined inter-particle distances (Tang et al. 2013) and can represent realistic particle shapes (Garcia-Hernandez et al. 2021a). Despite their potential, the widespread adoption of DEM and PE in the road industry remains limited.

This paper navigates a pioneering path toward evaluating the feasibility of pothole remediation through the integration of digital design techniques and autonomation. The paper's framework encompasses three phases: the development of an automated pothole filling machine (APFM) in phase one, the digital design of extrudable asphalt mixtures with a performance-based approach in phase two, and the validation of filled pothole durability in the final phase. Beside automated repairs, the insights from this study could potentially contribute to the creation of intelligent pavers that can independently choose aggregate and bitumen ratios to streamline asphalt production in the future.

2 Brief description of the proposed asphalt digital design, the automated pothole filling process and its prospects

Autonomous pothole repair combines digital design and machine automation for road surface pothole repair. This method begins with assessing pothole volume and selecting suitable asphalt grades. Optimisation includes understanding aggregate geometry and bitumen performance. This paper introduces a performance-based approach centred on aggregate shape. It starts with image-derived properties, estimating aggregate count and mastic volume within 250 g of asphalt using physics engine software. Correlations between aggregate geometry and performance parameters such as air voids, stability, flow, and asphalt extrudability are established. A nomograph is developed to define a feasible region meeting all requirements, guiding gradation selection. Generated aggregate gradations are used to produce asphalt cartridges for use by the APFM. An adapted 3D printer served as the APFM, heating cartridges for extrusion. For larger potholes, the APFM manoeuvres around contours, ensuring even asphalt distribution. Extruded volumes are compacted layer by layer to match pothole depth, aligning
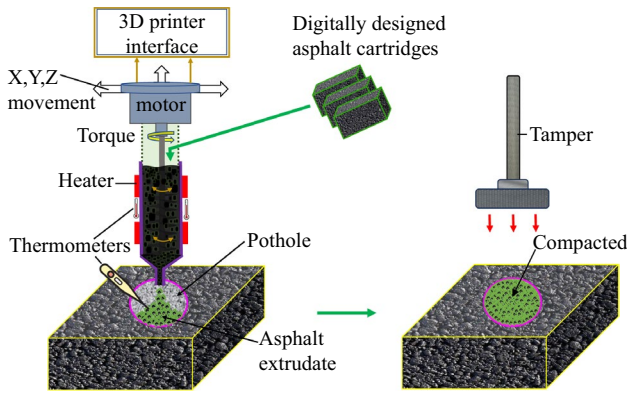
Fig. 1 Schematic illustration of the automated pothole filling process

with neighbouring road surface. Figure 1 provides a graphical representation of the pothole filling process.

An upscaled APFM can theoretically be attached to repair vehicles. The authors contend that automating pothole repair offers numerous benefits compared to traditional manual approaches. This method ensures heightened efficiency through continuous, fatigue-free operation and significantly reduces the risk of accidents and repetitive strain injuries in high-traffic areas. Moreover, it guarantees a uniform quality of work, unaffected by individual skill levels or subjective assessments, and reduces waste. Additionally, as the built environment transitions towards smart cities (Burlacu et al. 2022), the integration of such automated systems can promote a modern, adaptive, and efficient approach to managing urban transportation infrastructure.

3 Materials and methods

3.1 Aggregates and asphalt specimen

In this study, limestone aggregates were utilised in four distinct fractions: filler (0–0.125 mm), dust (0–4 mm), $L6$ (0–6.3 mm), and $L8$ (0–8.0 mm). The gradations for these fractions are detailed in Table 1. The fractions were combined to create aggregate gradations for both slab and pothole filling mixtures. Figure 2 displays the combined gradations for each specimen, and Table 2 presents detailed information on the asphalt mixture properties for the 34 blends used. All gradations maintained a nominal maximum aggregate size (NMAS) of 8 mm and an overall maximum size of 10 mm. The decision to use this maximum aggregate size was motivated by the aim to downsize the extruder on the APFM and thereby decrease its payload.

It is important to note that the choice of aggregate gradation was not driven by the desire to produce a specific asphalt type. Instead, the mixtures were selected randomly to encompass a wide spectrum of asphalt blends. The binder used in this study was bitumen penetration grade 40/60, a type frequently utilized in the United Kingdom. The bitumen exhibited a penetration of 43 mm and a softening point of 51.0 °C. Following the guidelines of BS EN 12697-35:2016 (British Standards Institution 2016), all asphalt mixtures were lab-prepared at 165 °C and compacted between 150 and 155 °C.

Table 1 Gradation of available aggregate fractions

Sieve size (mm)		10	8	6.3	4	2.8	2	1	0.5	0.25	0.125	0.063
$L8$	% Passing	100	64.48	20.64	1.85	1.21	1.15	1.14	1.13	1.12	1.1	1.07
$L6$		100	100	96.41	34.73	8.39	3.48	2.55	2.48	2.46	2.39	2.27
Dust		100	100	100	99.31	83.33	62.98	40.32	30.83	25.21	20.4	16.03
Filler		100	100	100	100	100	100	100	100	100	100	96.79

Fig. 2 Aggregate gradation for asphalt specimens: **a** specimens M1–M20, **b** specimens M21–M34, SMA limits and pothole slabs
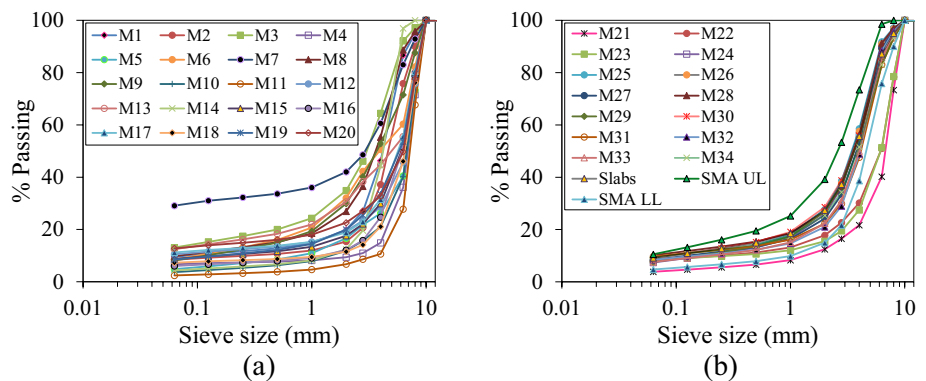
Table 2 Asphalt mixture properties

Mixture ID	Bitumen type	Compaction temperature (°C)	No. of blows	BC (%)	AVC (%)	Max. density (Mg/m³)
M1	PG 40/60	150.0	2×50	6.0	5.4	2.477
M2	PG 40/60	150.0	2×50	6.0	6.3	2.483
M3	PG 40/60	150.0	2×50	6.0	7.8	2.473
M4	PG 40/60	150.0	2×50	6.0	22.9	2.505
M5	PG 40/60	150.0	2×50	5.0	16.0	2.533
M6	PG 40/60	150.0	2×50	6.0	10.5	2.488
M7	PG 40/60	150.0	2×50	8.0	3.4	2.419
M8	PG 40/60	150.0	2×50	6.0	3.5	2.475
M9	PG 40/60	150.0	2×50	5.5	2.4	2.499
M10	PG 40/60	150.0	2×50	5.5	22.2	2.518
M11	PG 40/60	150.0	2×50	4.5	29.3	2.56
M12	PG 40/60	150.0	2×50	5.5	12.4	2.516
M13	PG 40/60	150.0	2×50	6.0	5.9	2.56
M14	PG 40/60	150.0	2×50	5.2	5.2	2.498
M15	PG 40/60	150.0	2×50	6.0	16.7	2.496
M16	PG 40/60	150.0	2×50	5.5	15.6	2.513
M17	PG 40/60	150.0	2×50	6.6	10.4	2.474
M18	PG 40/60	150.0	2×50	5.4	15.3	2.511
M19	PG 40/60	150.0	2×50	5.5	9.1	2.481
M20	PG 40/60	150.0	2×50	6.5	8.3	2.473
M21	PG 40/60	150.0	2×50	4.0	20.4	2.513
M22	PG 40/60	150.0	2×50	5.5	13.3	2.513
M23	PG 40/60	150.0	2×50	5.4	15.6	2.516
M24	PG 40/60	150.0	2×50	5.0	3.7	2.477
M25	PG 40/60	150.0	2×50	5.0	3.4	2.472
M26	PG 40/60	150.0	2×50	5.0	3.6	2.477
M27	PG 40/60	150.0	2×50	5.0	4.7	2.472
M28	PG 40/60	150.0	2×50	5.0	4.1	2.522
M29	PG 40/60	150.0	2×50	5.0	4.5	2.519
M30	PG 40/60	150.0	2×50	5.0	4.8	2.562
M31	PG 40/60	150.0	2×50	5.0	6.3	2.489
M32	PG 40/60	150.0	2×50	5.0	5.6	2.502
M33	PG 40/60	150.0	2×50	5.0	5.5	2.513
M34	PG 40/60	150.0	2×50	5.0	5.6	2.516
Slab	PG 40/60	150.0	Roller	5.5	4.0	2.492

3.2 Creation of asphalt cartridges

The manufactured hot loose asphalt mixtures were separated using a riffle technique before being placed within a Teflon mould. Following this, the upper surfaces of the specimens were levelled using a scraper. After allowing a cooling period of 30 min, the specimens were removed from the mould, resulting in cartridges with dimensions of 50–60 mm in length, 35 mm in width, and 16 mm in thickness. Samples of the fabricated cartridges are shown in Fig. 3.

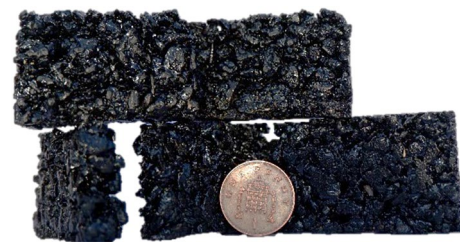These cartridges had a mass ranging approximately between 67.0 and 70.0 g. The volume of an individual

Fig. 3 Asphalt cartridges

cartridge was assessed by multiplying its mass by the asphalt target density. This estimation approach was then applied to determine the total number of cartridges required to effectively fill a pothole with specified dimensions.

3.3 Simulation of a pothole

A pothole was fabricated by combining two asphalt slabs. These slabs had dimensions of 305 mm by 305 mm. The upper slab, designated as the wearing course, had a thickness of 40 mm, while the base slab's thickness was 60 mm. This 40 mm thickness aligned with that of a moderately sized pothole (Miller and Bellinger 2014). The decision to opt for a 60 mm base thickness was motivated by the need to maintain a total specimen thickness of 100 mm to enable it to fit into the available Hamburg wheel tracking device described in Sect. 3.10.
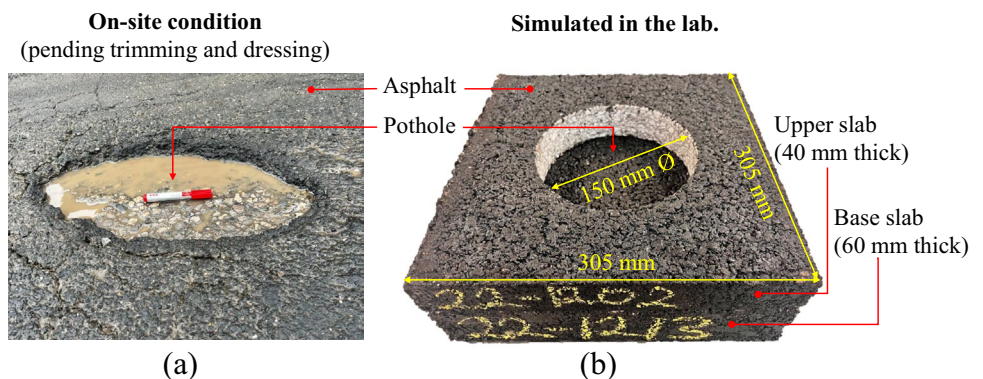
A hole with a diameter of 150 mm was extracted from the upper slab's centre. Following this, the hollow upper slab was firmly tack coated to the base slab using bitumen emulsion as an adhesive. This technique formed a pothole structure with a depth of 40 mm. The complete pothole assembly within the laboratory setting is depicted in Fig. 4b.

3.4 Estimation of air void content (AVC), Marshall stability, and Marshall flow

The method described in BS 12697-6-2020 (British Standard Institution 2020a) was used to evaluate the AVC of the asphalt mixtures. This technique involved a comparison between the bulk density of the asphalt and its theoretical maximum density, with any variation attributed to the presence of air voids.

Additionally, the Marshall Test following BS EN 12697-134:2020 (British Standards Institution 2020a) was used to create specimen cores and evaluate their stability and flow. The choice of the Marshall test was based on its simplicity and practicality. The standard testing temperature of 60 °C was selected to replicate the characteristics of the weakest Hot Mix Asphalt commonly observed in summertime.

3.5 Creation of virtual aggregates and virtual asphalt mixtures

Creating virtual aggregates began with image processing and analysis of sampled aggregates. Using ImageJ, properties like area, diameters, and height were assessed for over 120 aggregates per batch. Figure 5 visually represents some of the measured geometric properties, and Fig. 6 illustrates a virtual aggregate gradation for specimen 8. The geometric properties of aggregate fractions used in this study can be found in Table 3. Collected data led to Weibull curve fitting based on these parameters. Predictive rules depended on number of aggregates (NA) and volume of mastic (MV). Coarse aggregates (> 2 mm) were counted as those forming the asphalt solid skeleton, while fine aggregates (< 2 mm) and fillers (< 0.063 mm) combined with bitumen to form mastic. To ensure accurate counts, software generating 3D models with equivalent properties simulated complete gradations. A 2 mm aggregate limit was adopted due to challenges in extracting accurate geometric properties of fines
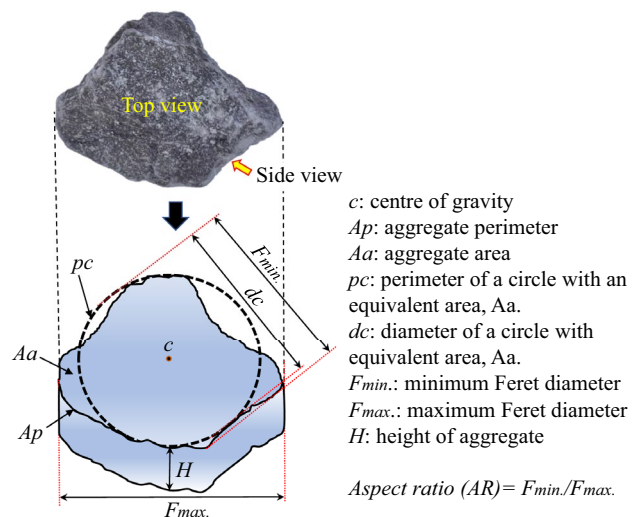

c: centre of gravity
Ap: aggregate perimeter
Aa: aggregate area
pc: perimeter of a circle with an equivalent area, Aa.
dc: diameter of a circle with equivalent area, Aa.
F_{min}.: minimum Feret diameter
F_{max}.: maximum Feret diameter
H: height of aggregate

Aspect ratio (AR)= $F_{min}./F_{max}.$

Fig. 5 Geometric projections of a typical 8 mm limestone aggregate

Fig. 4 Illustration of a pothole: **a** on-site condition, **b** lab simulated

On-site condition
(pending trimming and dressing)

Simulated in the lab.

(a)   (b)

Fig. 6 Virtual aggregate gradation example (specimen M8)

8 mm   6 mm   Dust (Min. Feret > 2 mm)
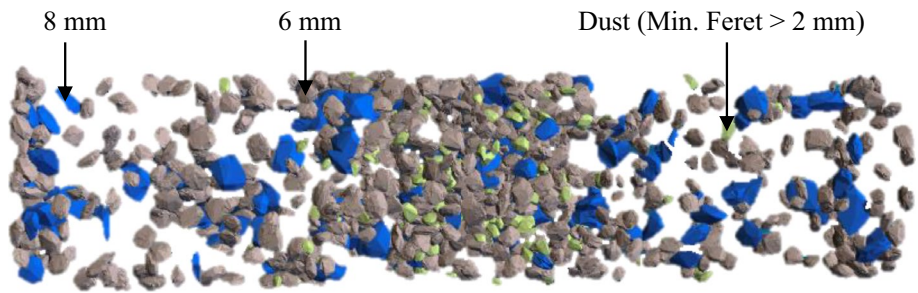
Table 3 Geometric and Weibull characteristics of aggregates

ID	Min Feret$_{50}$ (mm)	WSc Min Feret (mm)	WSh Min Feret	AR$_{50}$	WSc AR	WSh AR	A_{50} (cm^2)	P_{50} (cm)	H	% mass < 2 mm
LD	3.17	3.66	5.21	0.69	0.73	6.70	0.12	1.31	0.74	62.98
L6	8.72	5.30	3.90	0.68	0.77	7.37	0.23	1.81	0.61	3.48
L8	10.81	8.61	4.17	0.75	0.75	6.54	0.69	3.21	0.61	1.15

and fillers, and to minimise the number of virtual aggregates created, thereby accelerating simulation time.

The algorithm for creating virtual aggregates began by generating a cuboid matching minor and major Feret's diameters and height, within defined Weibull distributions. Points were distributed on the cuboid's surface and moved perpendicularly to mimic real aggregate surfaces. Virtual aggregates were defined by minor Feret's diameter, major Feret's diameter, height, point count, and distance from the cuboid surface. Further details of the virtual aggregate generation process can be found in reference (Garcia-Hernandez et al. 2021a, c).

3.6 Development of the hot-end screw-extrusion-based asphalt 3D printer (APFM)

In the laboratory simulation, a modified 3-axis screw-extrusion 3D printer was used as the APFM. The APFM contained an extruder which featured a 90 mm outer diameter × 100 mm long aluminium heating collar with a nozzle outlet having a nominal 30 mm through bore. The nozzle outlet incorporated a 316 stainless steel lever with an adjustable outlet gate valve. Housed within the collar was a 90 mm × 90 mm mica band heater rated at 24 V DC and 250 watts. An integral type K temperature sensor was situated close to the nozzle outlet to monitor the system's temperature, cross-validated regularly with an SPER Scientific 800115C thermometer.

A removable 200 mm diameter extension funnel, made of stainless steel, was positioned atop the collar to store surplus asphalt cartridges for seamless continuous extrusion. Inside the collar, a spiral feed screw with a 60 mm pitch and 60 mm

diameter facilitated the extrusion process. A 3 mm diameter and 20 mm tall circular peg was affixed to the centre screw blade to induce lateral stirring of mixtures during extrusion, ensuring even heating and minimizing stripping. The feed screw was linked to a Mclennan 1308-12-100 geared 100:1 DC motor capable of a maximum torque of 0.4 Nm and a no-load speed of 35 rpm. For safety, the heating collar was encased in an insulating jacket.

This extruder setup was integrated with an existing RepRap original Prusa i3 MK3S 3D printer. The selection of a RepRap was driven by its substantial payload capacity. A connected computer, aided by 3D printing software, allowed control over extruder movement in the X, Y, and Z directions, heating management, and asphalt extrusion at
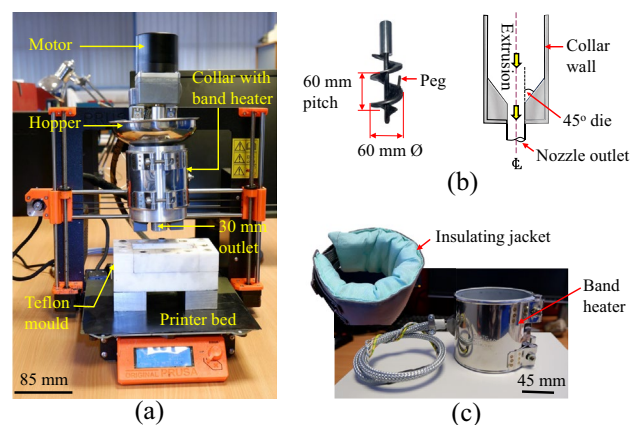

Fig. 7 Illustration of the asphalt 3D printer: **a** extruder mounted onto 3D printer frame, **b** spiral feed screw and die angle, **c** band heater and insulating jacket

screw speeds ranging from 1 to 36 rpm. Figure 7 showcases the APFM setup and its components.

3.7 Optimisation of the operational paramaters of the APFM

The critical operational parameters of the printer encompassed the DC power, extrusion rate, and extrusion temperature. The optimisation of the maximum power involved a trade-off between torque and extrusion speed, as depicted in Fig. 8. The DC motor possessed a maximum torque of 0.4 Nm and a no-load speed of 35 rpm. Electric motor torque signifies the rotational force generated by the motor. The maximum power was estimated through a speed-torque optimisation, resulting in the largest area beneath the speed-torque curve. From the graphical representation in Fig. 8a, the optimised coordinates intersected at the midpoint of speed and torque, specifically at 0.5 τ_s and 0.5 ω_n. Using this relationship, a maximum power of about 0.366 kW was attained using Eq. (1), with a torque of 0.2 Nm and a speed of 17.5 rpm.

$$P = \frac{2\pi \cdot \tau \cdot \omega}{60} \tag{1}$$

Here, P represents power in kW, τ denotes torque in Nm, and ω signifies speed (angular velocity) in rpm.

Furthermore, in an experiment investigating the impact of extrusion speed on extrusion rate using specimen M8, an optimal speed of 16–18 rpm was identified, as indicated in Fig. 8b. This experimentally verifies the estimated optimal speed of 17.5 rpm as deduced from Fig. 8b.

The extrusion die angle was also a crucial consideration in the extrusion process, as it significantly influenced the flow of asphalt material. This angle not only affected extrusion force but also influenced defects in extrudates due to friction and uneven material flow. A lower die angle, for instance, introduced more friction at the asphalt-die interface. Consequently, an optimised die angle of 45 °C was adopted to enhance the efficiency and effectiveness of the extrusion process, while mitigating concerns such as material flow resistance, clogging, and excessive wear (Lebaal et al. 2009; Gbenebor et al. 2013).

Additionally, it was observed that extrudates were approximately 6 °C cooler than the programmed band heating. This temperature drop was anticipated due to heat losses to the surroundings as the extrudate exited the nozzle outlets. Importantly, since asphalt mixtures were extruded at 165 °C with a targeted compaction temperature of 150 °C, the variance was not a significant concern.

Lastly, a circular outlet shape was selected for its simplicity. It is important to note that as the cross-section becomes more intricate, higher pressure and greater extrusion force would be necessitated.

3.8 The extrusion and filling process

The extruder nozzle of the APFM operated based on specified pothole coordinates. These coordinates were obtained through the capturing and processing of top-view vector images of the potholes in the open-source Inkscape software. By utilising the 'object to path' tool, the geometric path coordinates were converted to G-codes for use in the 3D printing software. The designated filling path was set 30 mm from the pothole's edges, initiating a circular route until the brim was reached, after which the centre was filled. This strategy ensured a consistent distribution of materials, making it easier to achieve comprehensive coverage during the compaction process.

Prior to extrusion, asphalt cartridges were preheated at 60 °C for 30 min, and the extrusion collar system was preheated at 171 °C for 10 min to ensure uniform temperature. Extrusion rate measurements were conducted by gradually feeding asphalt cartridges into the collar while rotating the screw at 2 rpm to fully load the collar (mixing chamber) with the nozzle closed. When the collar is full, the nozzle is opened, and at a screw speed of 18 rpm, the volume of asphalt extruded in 10 s was recorded. This process was repeated three times per specimen, and the extrudate volume was determined from mass and target density. Given similar

Fig. 8 Optimisation of the operational parameters of a DC motor: **a** maximising operating power, **b** optimising extrusion speed using mixture M8
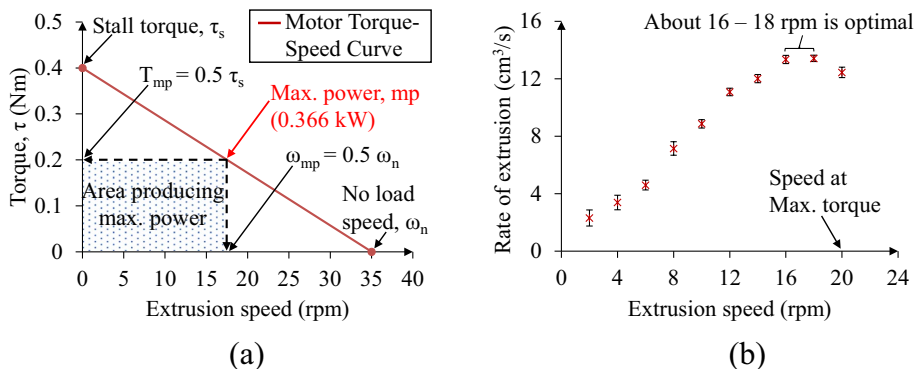
asphalt densities, density variations had negligible impact on extrusion rate estimations. Also, expressing extrusion rate in cm^3/s quantified asphalt needed to fill a certain pothole volume in a specific time.

3.9 Compaction of asphalt in potholes

Following the extrusion of the required asphalt volume into potholes with tack-coated walls, manual compaction was carried using a 2.5-kg compaction rammer. A 150-mm diameter iron plate, heated to 150 °C, was placed on top of the to be compacted mixture to create a level surface. Given that the targeted density was estimated based on the pothole's volume of 515 cm^3, compacting the asphalt to a depth of 40 mm was necessary to achieve the desired density.

3.10 Simulating traffic and evaluating filled pothole quality

Traffic simulation was conducted using a small-sized Hamburg Wheel Tracking device (Cooper, Ripley, UK) following procedure B in accordance with BS EN 12697-22:2020 (British Standard Institution 2020b). The goal was to assess the resistance of the filled potholes to permanent deformation under cyclic loading in soaked conditions. Asphalt samples, measuring 305 mm × 305 mm × 100 mm (including a 150 mm Ø × 40 mm deep filled pothole in the upper slab), were fully submerged in water at 30 °C ± 1.

The wheel, running at approximately 26.7 rpm with an applied load of 705 ± 4.5 N, tracked at 10,000 cycles per test. Each cycle consisted of two passes. A lower temperature of 30 °C was chosen to prevent excessive rutting of the pothole filling materials in comparison to the surrounding asphalt. Test specimens were temperature-conditioned at 30 °C for 12 h to ensure temperature equilibrium within the specimens. For each case scenario, two parallel specimens were tested to enhance the reliability of the results. The reported final rut depths represent the mean rut depths of the two parallel specimens.

Additionally, 100 mm cores were extracted from parallel filled pothole specimens to estimate the AVC following reference (British Standard Institution 2020a). The measured AVC values were then compared to the targeted AVC values.

3.11 Pothole filling by hand

In the laboratory, parallel potholes were manually filled to replicate on-site pothole patching methods for comparison with automated fills. This entailed producing asphalt with identical gradations and recipes as those used for the automated fills. The primary distinction was that loose hot asphalt mixtures were poured directly into the potholes at once. Like the automated fills, the poured asphalt was compacted using a tamper to align with the surrounding asphalt.

4 Results and discussion

4.1 Properties of the asphalt mixtures

Table 4 displays the experimental outcomes and the computed NA and MV for the 34 mixtures used in this study (M1–M34). Each value reflects the results from three experiments or numerical simulations. These mixtures displayed significant variation, spanning from porous to dense asphalt

Table 4 Simulated and experimental characteristics of asphalt mixtures

Mixture ID	MV (cm^3)	NA	E (cm^3/s)	S (kN)	F (mm)
M1	31.8	1268	85.5	7.7	1.7
M2	27.8	1129	101.1	6.8	1.4
M3	44.9	1283	57.9	11.7	7.1
M4	22.6	522	160.6	7.1	1.2
M5	26.7	655	90.7	8.3	1.8
M6	42.4	874	64.3	10.9	5.8
M7	55.1	869	48.9	14.5	9.3
M8	37.9	1272	70.9	10.1	3.0
M9	39.5	1087	71.1	9.1	4.0
M10	23.6	664	144.8	7.7	1.8
M11	17.3	510	213.8	6.6	1.0
M12	30.2	614	79.2	9.3	1.8
M13	41.1	750	82.4	9.2	3.2
M14	23.4	1537	141.1	7.5	1.4
M15	23.8	722	153.7	8.6	1.5
M16	23.8	802	162.7	7.6	1.4
M17	32.2	753	97.2	9.1	2.1
M18	27.0	681	103.7	8.0	1.1
M19	30.7	775	96.4	9.7	1.7
M20	35.2	647	69.2	8.5	3.4
M21	20.7	710	152.6	7.7	1.2
M22	28.8	693	87.5	7.4	2.0
M23	26.6	676	85.1	7.5	1.7
M24	34.8	1342	67.0	10.2	3.0
M25	36.5	1357	63.0	10.5	3.5
M26	35.91	1348	13.1	10.2	3.3
M27	33.36	1295	11.2	9.7	3.1
M28	35.74	1316	13.3	9.9	3.6
M29	35.78	1251	13.5	10.1	3.6
M30	37.26	1196	13.6	10.4	3.6
M31	31.64	1202	9.2	9.8	2.6
M32	30.52	1303	10.4	9.6	2.4
M33	31.80	1285	11.2	9.8	2.4
M34	34.40	1206	12.5	10.6	3.1

compositions. As a result, Extrudability (*E*), Marshall stability (*S*), and Marshall flow (*F*) exhibited a broad spectrum of results. This approach was adopted to ensure that the models do not become excessively tailored to particular mixtures, thereby avoiding overfitting.

The data in Table 4 are used for further statistical analysis to identify any potential relationships between the performance parameters. These statistical correlations facilitated the determination of optimal mixture compositions.

4.2 Relationships between asphalt performance parameters, volume of mastic, and number of aggregates

Equation (2) serves as the predictive model for the examined performance parameters in Table 4. This rational equation is derived from the Weibull equation and has been chosen based on its demonstrated ability in the previous studies (Garcia-Hernandez et al. 2021c; Aboufoul et al. 2019) to effectively capture a variety of emerging asphalt properties influenced by aggregate gradation. These properties include hydraulic conductivity and the compaction force needed for asphalt materials.

$$\text{Performance parameter} = \frac{a + b\text{MV} + c\text{NA}}{1 + d\text{MV} + e\text{NA}}, \quad (2)$$

where *a*, *b*, *c*, *d*, *e* are constants; MV is volume of mastic (cm^3) and NA is number of aggregates.

Table 5 presents the fitting parameters for Eq. (2) in relation to *E*, *S*, *F*, and AVC. The table also evaluates the goodness of fit for these parameters. Across all four instances, the *R*-squared (R^2) values either meet or surpass 0.80, signifying that NA and MV jointly account for more than 80% of the input variations in each scenario. It is noteworthy that there are no significant disparities between the R^2 and adjusted *R*-squared (adjusted R^2) values, emphasising the substantial significance of these two independent variables. The close concurrence between R^2 and adjusted R^2 values further reinforces the notion that the prediction of the performance parameters is not a random occurrence but rather a robust and reliable outcome.

As detailed in Eq. (2), the performance parameter is a function of NA and MV. The relationships in Table 5 can be illustrated graphically to visualise the trends. Figure 9 gives an example illustration for *E* and *S*. Both Table 5 and Fig. 9 indicate that NA and MV strongly influence the *E*, *S*, *F*, AVC of asphalt mixtures. However, it is important to note that the analysis is based on only 34 results, which is insufficient to draw definitive conclusions regarding the use of this relationship for predicting asphalt performance. Nonetheless, these findings provide valuable insights for future studies, highlighting the potential inputs that need to be considered. It is also important to acknowledge that these results do not take into account various factors such as different types of bitumen, compaction temperatures, and compaction energies.

Table 5 Parameters for the fitting equations, goodness of fit and design limits

Performance	Fitting equation	R^2	Adj. R^2	RMSE	Design limits
E (cm^3/s)	$E = \frac{-4.344 + 4.206\times10^{-1}\text{MV} - 2.669\times10^{-3}\text{NA}}{1 + 3.042\times10^{-3}\text{MV} - 4.211\times10^{-4}\text{NA}}$	0.89	0.89	1.53	> 10
S (kN)	$S = \frac{5.865 - 2.031\times10^{-3}\text{MV} - 1.140\times10^{-3}\text{NA}}{1 - 9.176\times10^{-3}\text{MV} - 6.831\times10^{-5}\text{NA}}$	0.78	0.78	0.75	> 6.7
F (mm)	$F = \frac{0.157 + 4.234\times10^{-2}\text{MV} - 5.330\times10^{-4}\text{NA}}{1 - 1.000\times10^{-2}\text{MV} - 1.096\times10^{-4}\text{NA}}$	0.99	0.99	0.12	2–4
AVC (%)	$F = \frac{1.127\times10^9 - 6.767\times10^6\text{MV} - 5.161\times10^5\text{NA}}{1 + 1.454\times10^6\text{MV} + 205\text{NA}}$	0.94	0.94	1.73	3–5

Fig. 9 Relationship between number of aggregates, volume of mastic and: **a** extrudability, **b** stability
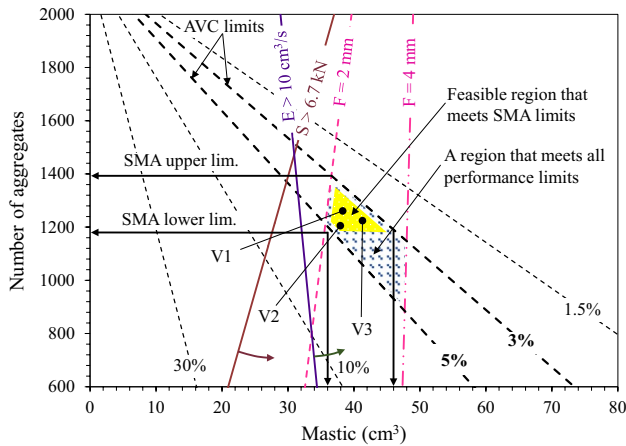

(a)

(b)
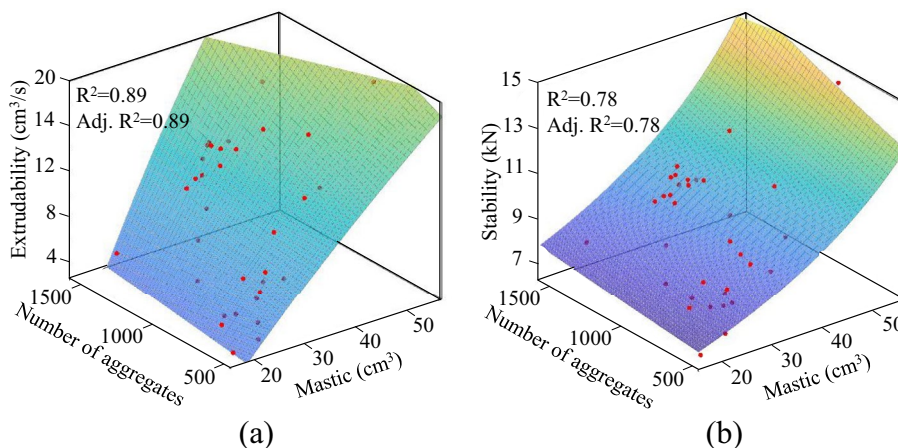
Fig. 10 Nomograph for the design of asphalt

4.3 Creating a nomograph for asphalt design

The performance parameter boundaries, established by the authors and detailed in Table 5, delineate the focal area for the asphalt design in this study. These thresholds, grounded in experimental knowledge and corroborated by British Standards Institution (2020b) and Main Roads Western Australia (2022), are visualised in the nomograph in Fig. 10, which assists in selecting appropriate NA and MV values that comply with Table 5 limits.

Figure 10 shows the relationship between the performance metrics of asphalt mixtures, the NA and the MV. It points out that a reduction in MV amplifies the porosity of the mixtures, while maintaining an MV above 34 cm^3 is vital to achieve a minimum extrusion rate of 10 cm^3/s with the APFM. Furthermore, a higher mastic quantity tends to enhance the flow in the asphalt mixtures.

In the spiral-feed-screw extrusion process, an MV aids in increasing the extrusion rate by effectively lubricating the interaction between the asphalt bigger aggregates and the collar-screw walls. The mastic also potentially enhances the moldability along the extrusion path. On the flip side, mixtures containing a higher proportion of NA tend to exhibit increased internal friction and stresses, thereby reducing the rate of extrusion. It should be mentioned that this study maintained the same bitumen type in all mixtures, hence it did not examine the influence of fluctuating temperatures on the extrudability of the mixtures.

"A region that meets all performance limits" has been delineated in Fig. 10, highlighting the intersection of NA and MV within which asphalt is expected to obey the design limits in Fig. 5. Moving forward, the delineated performance boundary could be further narrowed based on specific mixture classifications, including dense asphalt, open-graded, SMA, among others. This categorisation involves using the NA and MV within the upper and lower limits of the desired

mixture. The limits of an SMA have been adopted in this study and used to create a subregion within the performance boundary. This subregion represents a feasible region consisting of SMA mixtures that conform to all design rules specified in Table 5. Within this viable realm, selecting any MV–NA coordinate pair (along the x and y axes) will guide the selection of suitable aggregate gradation for the creation of an extrudable yet durable SMA mixture. Section 4.4 details how different aggregate gredations were iteratively generated from the feasible region in Fig. 10.

4.4 Iterations for generating aggregate gradations from the nomograph

The study validates the nomograph by verifying if it can correctly produce aggregate gradations based on selected NA and MV contents. The gradation selection is based on an assumed 5% bitumen content (BC) in a 250 g asphalt sample.

The aggregate fractions available in the laboratory for manufacturing asphalts (filler (Lf), dust (LD), L6 and L8) were individually analysed to determine the NA and MV with the 5% bitumen content. Note that the AVC of a mixture does not influence its aggregate count. Additionally, when keeping the bitumen volume constant and using the same aggregate fraction, the MV in a specified mass of specimen remains unchanged. Table 6 presents the values for each aggregate fraction, which can be combined with Eqs. (3) and (4) to design new asphalt mixtures. In a mixture with only filler aggregates, for example, no NA will be recorded making the entire composition 100% mastic. Table 6 shows the number of aggregates and volume of mastic for the 250 g of each aggregate fraction. The limit range for the NA (1179–1394) and mastic volume (38–46 cm^3) is defined by the SMA limits as illustrated in Fig. 10.

More specifically, three mixtures have been selected randomly for the aggregate generation, mixtures V1, V2, and V3. The corresponding MV and NA coordinates for these mixtures have been shown in Fig. 10 and detailed in Table 7.

Table 6 Number of aggregates and volume of mastic for different fractions of aggregates, SMA limits and feasible region bounds

ID	Proportion of aggregate (ϕ)	MV (cm^3)	NA
L_8	ϕ_{L8}	13.01	375
L_6	ϕ_{L6}	15.08	1582
L_D	ϕ_{LD}	25.2	1269
L_f	ϕ_{Lf}	100	0
SMA (upper)		46.6	1394
SMA (lower)		25.2	1179
Feasible region		38–46	1179–1394

Table 7 Number of aggregates and volume of mastic for selected coordinates on the nomograph

Mixture ID	MV (cm³)	NA
V1	39.05	1284
V2	38.07	1213
V3	41.71	1231

An optimisation algorithm was developed in Microsoft Excel to calculate the proportions of aggregates (ϕ) required to produce values of the aggregates fractions (ϕ_{L8}, ϕ_{L6}, ϕ_{LD}, ϕ_{Lf}) that meets the NA and MV based on minimising squared errors. An example of this is shown in Eqs. (3) and (4) for illustration of mixture V1's optimisation. For complex iterations in future studies, machine learning applications may be utilised. The optimisation equations estimated 100% NA and MV compared to quantities generated with the algorithm. With the NA and MV estimated, the corresponding performance parameters can be estimated using Eq. (2).

Equation for the volume of mastic for specimen V1:

$$13.01\phi_{L8} + 15.08\phi_{L6} + 67.62\phi_{LD} + 100\phi_{Lf} = 39.05 \text{ cm}^3 \tag{3}$$

Equation for the number of aggregates for specimen V1:

$$375\phi_{L8} + 1582\phi_{L6} + 1269\phi_{LD} + 100\alpha_{Lf} = 1284 \tag{4}$$

where ϕ_{L8}, ϕ_{L6}, ϕ_{LD}, and ϕ_{Lf} represent the respective proportions (in percentage) of 8 mm aggregates, 6 mm aggregates, limestone dust, and limestone filler in the final gradation.

The required proportions of aggregate fractions, determined through iterations to yield the specified NA and MV quantities, are detailed in Table 8. Additionally, Fig. 11 displays the combined gradations of these fractions used to create various mixtures (V1, V2, and V3). The boundaries of the SMA specifications are illustrated in Fig. 11 to delineate the position of the validation mixtures within the SMA envelope.

4.5 Comparison of nomograph-generated and experimentally tested asphalt mixture performances

The subsequent procedure entailed the production of laboratory asphalt samples V1, V2, and V3, utilising the simulated

Table 8 Generated gradations for validation of nomographs

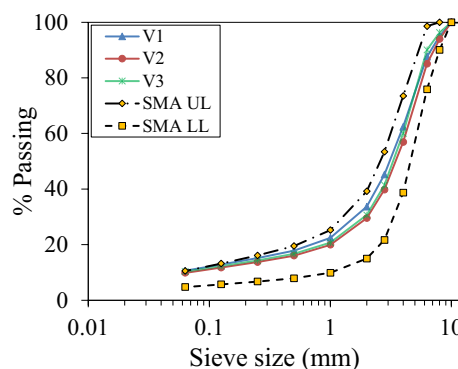| Mixture ID	Aggregate proportion (ϕ)			
	L_8	L_6	L_D	L_f
V1	10.5	45	42	2.5
V2	17	40	40.7	2.3
V3	14	36	48	2.0

Fig. 11 Cumulative gradations for generated aggregates compliant with BS EN 13108-5:2016 (British Standards Institution 2020b)

aggregate gradations presented in Table 8 with a 5% bitumen content. The targeted porosity was determined based on the nomograph AVC estimates. The maximum densities achieved for V1, V2, and V3 were 2.438 Mg/m³, 2.471 Mg/m³, and 2.522 Mg/m³, respectively. The E, S and F of various mixtures were also experimentally measured. Table 9 presents a comparison between the predicted values obtained from the nomograph approach proposed in this study and the experimentally measured values. Predictivity is expressed as a percentage of the relative error between the predicted and measured values. On average, the nomograph demonstrated an error rate of 8.0%, corresponding to a prediction rate of 92.0%.

4.6 Pothole filling and evaluation of filling quality

Mixtures V1 and V2 were randomly selected for filling the lab-simulated potholes using both the developed APFM and by hand. Figure 12 presents the deformation profiles of the filled potholes and offers a comparison between the automated and manual filling approaches. Table 10 provides data on final rut depths and corresponding AVC values. Notably, V1 fills exhibit lower rutting resistance due to their lower stability and higher flow characteristics (as indicated in Table 9). With a mean rut depth error percentage of 14.4% as indicated in Table 10, automated fills are projected to provide 85.6% of the rutting resistance observed in manual fills. The superior rutting resistance in manual fills can be attributed to more effective compaction, leading to reduced AVC deviations. This happens because automated fills, compacted in layers, can trap air, increasing porosity. Meanwhile, manual fills, compacted in a single pour, achieve better aggregate packing throughout the pothole depth.

Positively, automated-filled potholes show about 86% of the traffic endurance seen in manual fills, indicating a promising future for the automated techniques in both research and practice. Improving compaction and extrudate cooling

Table 9 Predictivity of performance of asphalt designed with the monograph

Mixture ID	Parameter	Nomograph (p)	Experimental (m)	Absolute error ($m - p$)	% error $[(m - p)/m] \times 100$
$V1$	E, cm^3/s	15.0	15.8	0.8	5.3
	S, kN	7.8	7.2	0.6	8.4
	F, mm	2.4	2.6	0.2	7.6
	AVC, %	3.5	3.9	0.4	10.1
$V2$	E, cm^3/s	13.9	14.5	0.6	3.9
	S, kN	7.8	8.6	0.8	9.8
	F, mm	2.3	2.5	0.2	7.7
	AVC, %	4.4	4.8	0.4	8.8
$V3$	E, cm^3/s	16.3	15.7	0.6	3.8
	S, kN	8.2	8.7	0.5	5.6
	F, mm	2.8	3.1	0.3	8.8
	AVC, %	3.4	4.1	0.7	16.1
Average error	E, cm^3/s			0.7	4.3
	S, kN			0.6	7.9
	F, mm			0.2	8.0
	AVC, %			0.6	13.5
Mean % error					8.0
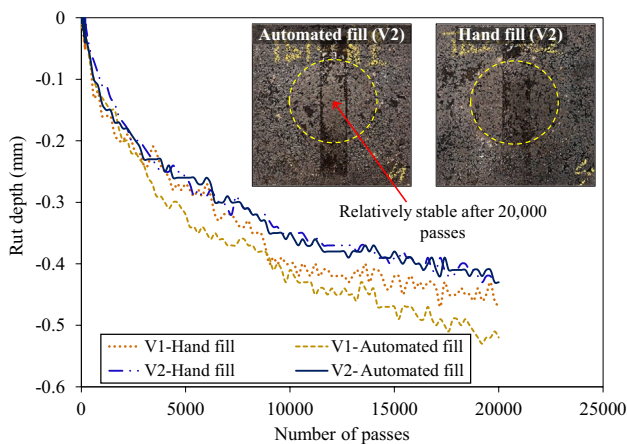
Fig. 12 Comparing rutting resistance in filled pothole specimens: automated and hand filling

could enhance future automated pothole repairs; hence, subsequent studies could investigate the use of extrudable self-compacting asphalt mixtures for enhanced performance.

4.7 Limitations of the study

An NMAS of 8 mm was used to downsize the extruder on the APFM, constraining its usability. A larger NMAS needs to be considered in future applications. Additionally, although the digital design method demonstrated in this paper can accurately predict asphalt performances, it is important to note that the study solely focuses on mixtures compacted at uniform temperatures and energy levels. The generalisability of this design method to asphalt mixtures that requires different compaction energies remains uncertain. To address this limitation, future research endeavours should consider the utilisation of machine learning techniques to enhance prediction capabilities across varying compaction levels. Moreover, the paper does not address the automation of the compaction process due to its complexity in integrating it with a simple APFM, and the asphalt extrudate in the potholes were compacted with an isolated tamper as illustrated in Fig. 1. Further research is required, particularly on the upscaling of the APFM, to explore more efficient methods of achieving the required densities of asphalt extrudates in

Table 10 Wheel tracking test results comparing the rutting resistance of automated and hand filled pothole specimens

Specimen ID	AVC (%)		Final rut depth (mm)		Avg. absolute error ($h - a$)	% error $[(h - a)/h] \times 100$
	Automated	Hand	Automated (a)	Hand (h)		
$V1$	4.3	3.8	0.39	0.33	0.06	18.2
$V2$	5.1	4.6	0.52	0.47	0.05	10.6
			Rut depth mean % error			14.4

potholes. The use of self-compacting asphalt mixtures could be a good starting point.

5 Conclusions

This experimental study aimed to revolutionise pothole repair by integrating the digital generation of asphalt cartridges and automated filling processes using an automated pothole filling machine that demands minimal human intervention. Lab-simulated potholes were filled both by the machine and by hand, and their durability was compared through wheel tracking tests. The following conclusions were drawn:

- A new digital performance-based method for advancing the selection of aggregate and bitumen proportions for the creation of asphalt cartridges have been demonstrated. The method exhibited 92% accuracy in developing mixtures that meet specified extrusion rates for enhanced productivity whilst achieving standard Marshall stability, Marshall flow, and air void content performances.
- In the laboratory setting, a simple-to-use 3-axis screw-extrusion 3D printer served as the machine. This machine could navigate pothole contours while extruding asphalt into lab-simulated potholes at the required temperature and speed.
- Asphalt extrusion rates (expressed in cm^3/s) were enhanced with maximised motor power (0.366 kW) achieved by operating at an optimised extrusion speed of 18 rpm and a motor torque of 0.2 Nm. These findings underscore the need to carefully optimise in order to customise extrusion speeds in future automated pothole filling machines to achieve highest asphalt extrusion rate values.
- Comparing manual and automated pothole filling techniques revealed that manual fills exhibited superior rutting resistance due to more effective compaction. Nevertheless, automated filling demonstrated promising potential, achieving 86% of the rutting resistance observed in manual fills. This underscores the feasibility of automation as a viable alternative to current manual methods.

The findings of this study also highlight the potential for the development of intelligent asphalt paving machines capable of autonomously selecting asphalt recipes according to desired functionalities, manufacturing them, and applying the asphalt mixtures in defect repairs. Future research should focus on scaling up this technology with fully autonomous systems integrated throughout the pothole repair process for in-situ trials.

Declarations

References

Aboufoul M, Chiarelli A, Triguero I, Garcia A (2019) Virtual porous materials to predict the air void topology and hydraulic conductivity of asphalt roads. Powder Technol 352:294–304. https://doi.org/10.1016/j.powtec.2019.04.072

Awuah FKA, Garcia-Hernández A (2022) Machine-filling of cracks in asphalt concrete. Autom Constr 141:104463. https://doi.org/10.1016/j.autcon.2022.104463

British Standard Institution (2020a) BS EN 12697-6-2020, bituminous mixtures—test methods, determination of bulk density of bituminous specimens. https://bsol.bsigroup.com/Search/Search?searchKey=BS+EN+12697.6%3A2020&OriginPage=Header+Search+Box&autoSuggestion=false. Accessed 16 May 2023

British Standard Institution (2020b) BS EN 12697-22:2020, bituminous mixtures—test methods, wheel tracking. https://bsol.bsigroup.com/PdfViewer/Viewer?pid=000000000030371556. Accessed 12 Sept 2023

British Standards Institution (2016) Bituminous mixtures—test methods, part 35: laboratory mixing (BS EN 12697-35:2016). https://bsol.bsigroup.com/PdfViewer/Viewer?pid=000000000030310362. Accessed 2 Aug 2022

British Standards Institution (2020) BS EN 12697-34:2020, bituminous mixtures—test methods, part 34: Marshall test. https://bsol.bsigroup.com/PdfViewer/Viewer?pid=000000000030382720. Accessed 22 Nov 2022

British Standards Institution (2020b) BS EN 13108-1:2016, bituminous mixtures—material specifications—part 1: asphalt concrete. https://bsol.bsigroup.com/PdfViewer/Viewer?pid=000000000030410633. Accessed 22 Nov 2022

Bruno S, Loprencipe G, Di Mascio P, Cantisani G, Fiore N, Polidori C, D'Andrea A, Moretti L (2023) A robotized Raspberry-based system for pothole 3D reconstruction and mapping. Sensors 23:5860. https://doi.org/10.3390/s23135860

Burlacu M, Boboc RG, Butilă EV (2022) Smart cities and transportation: reviewing the scientific character of the theories. Sustainability (switzerland) 14:8109. https://doi.org/10.3390/su14138109

Changra A, Singh EG (2023) Comparison of Marshall Stability values of the different bitumen mixes with crumb rubber. IOP Conf Ser Earth Environ Sci 1110:012034. https://doi.org/10.1088/1755-1315/1110/1/012034

Davila Delgado JM, Oyedele L, Ajayi A, Akanbi L, Akinade O, Bilal M, Owolabi H (2019) Robotics and automated systems in construction: understanding industry-specific challenges for adoption. J Build Eng 26:100868. https://doi.org/10.1016/j.jobe.2019.100868

Eskandari Torbaghan M, Kaddouh B, Abdellatif M, Metje N, Liu J, Jackson R, Rogers CDF, Chapman DN, Fuentes R, Miodownik M, Richardson R, Purnell P (2019) Robotic and autonomous systems for road asset management: a position paper. In: Proceedings of the Institution of Civil Engineers—smart infrastructure and construction, vol 172, pp 83–93. https://doi.org/10.1680/jsmic.19.00008

García de Soto B, Agustí-Juan I, Hunhevicz J, Joss S, Graser K, Habert G, Adey BT (2018) Productivity of digital fabrication in construction: cost and time analysis of a robotically built wall. Autom Constr 92:297–311. https://doi.org/10.1016/j.autcon.2018.04.004

Garcia-Hernandez A, Michot-Roberto S, Dopazo-Hilario S, Chiarelli A, Dawson A (2021a) Creation of realistic virtual aggregate avatars. Powder Technol 378:760–771. https://doi.org/10.1016/j.powtec.2020.10.036

Garcia-Hernandez A, Wan L, Dopazo-Hilario S, Chiarelli A, Dawson A (2021b) Generation of virtual asphalt concrete in a physics engine. Constr Build Mater 286:122972. https://doi.org/10.1016/j.conbuildmat.2021.122972

Garcia-Hernandez A, Wan L, Dopazo-Hilario S (2021c) In-silico manufacturing of asphalt concrete. Powder Technol 386:399–410. https://doi.org/10.1016/j.powtec.2021.03.065

Gbenebor OP, Fayomi OSI, Popoola API, Inegbenebor AO, Oyawale F (2013) Extrusion die geometry effects on the energy absorbing properties and deformation response of 6063-type Al-Mg-Si aluminum alloy. Results Phys 3:1–6. https://doi.org/10.1016/j.rinp.2013.01.002

Gong F, Cheng X, Fang B, Cheng C, Liu Y, You Z (2023) Prospect of 3D printing technologies in maintenance of asphalt pavement cracks and potholes. J Clean Prod 397:136551. https://doi.org/10.1016/j.jclepro.2023.136551

Gul MA, Islam MK, Awan HH, Sohail M, Al Fuhaid AF, Arifuzzaman M, Qureshi HJ (2022) Prediction of Marshall stability and Marshall flow of asphalt pavements using supervised machine learning algorithms. Symmetry (basel) 14:2324. https://doi.org/10.3390/sym14112324

Ipavec A (2012) POTHOLE: study of existing standards, techniques, materials and experience with them on the European market. https://www.cedr.eu/download/other_public_files/research_programme/eranet_road/call_2011/design/pothole/03_pothole_d3-techniques-and-materials-study.pdf. Accessed 12 Sept 2023

JCB (2023) JCB Pothole Pro—efficient & safe road pothole & street repairs. https://www.jcbcea.com.au/2023/06/revolutionising-roadworks-unveiling-the-jcb-pothole-pro-the-ultimate-solution-for-efficient-and-safe-pothole-repairs/. Accessed 12 Sept 2023

Karelina MY, Vasiliev AV, Guly VV, Podgorny AV, Erpulev VA (2022) Robotic systems in road construction. In: 2022 systems of signals generating and processing in the field of on board communications, SOSG 2022—conference proceedings. Institute of Electrical and Electronics Engineers Inc. https://doi.org/10.1109/IEEECONF53456.2022.9744273

Katsamenis I, Bimpas M, Protopapadakis E, Zafeiropoulos C, Kalogeras D, Doulamis A, Doulamis N, Montoliu CM-P, Handanos Y, Schmidt F, Ott L, Cantero M, Lopez R (2023) Robotic maintenance of road infrastructures: the HERON Project. http://arxiv.org/abs/2205.04164

Kwon BJ, Kim D, Rhee SK, Kim YR (2018) Spray injection patching for pothole repair using 100 percent reclaimed asphalt pavement. Constr Build Mater 166:445–451. https://doi.org/10.1016/j.conbuildmat.2018.01.145

Lebaal N, Schmidt F, Puissant S, Schlaefli D, Schläfli D (2009) Design of optimal extrusion die for a range of different materials. Polym Eng Sci 49:432–440. https://doi.org/10.1002/pen.21298ï

Liu P, Xing Q, Wang D, Oeser M (2018) Application of linear viscoelastic properties in semianalytical finite element method with recursive time integration to analyze asphalt pavement structure. Adv Civ Eng 2018:1–15. https://doi.org/10.1155/2018/9045820

Main Roads Western Australia (2022) Specification 504: asphalt wearing course. https://www.mainroads.wa.gov.au/globalassets/technical-commercial/technical-library/specifications/500-series-pavements/specification-504-asphalt-wearing-course.pdf. Accessed 22 Nov 2022

Von Mammen S, Gerling V (2016) Robotics for self-organised construction. https://doi.org/10.1109/FAS-W.2016.45

Manuel Davila Delgado J, Oyedele L (2022) Robotics in construction: a critical review of the reinforcement learning and imitation learning paradigms. Adv Eng Inform 54:101787. https://doi.org/10.1016/j.aei.2022.101787

Mchale MJ, Nicholls JC, Carswell I, Carswell I (2016) TRL RN44: best practice guide for the selection of pothole repair options. https://www.transport.gov.scot/media/4706/rn44-best-practice-guide-for-the-selection-of-pothole-repair-options.pdf. Accessed 12 Sept 2023

Miller JS, Bellinger WY (2014) FHWA-HRT-13-092: distress identification manual for the long-term pavement performance program. https://www.fhwa.dot.gov/publications/research/infrastructure/pavements/ltpp/13092/13092.pdf. Accessed 12 Sept 2023

O'Sullivan C, Bray JD (2004) Selecting a suitable time step for discrete element simulations that use the central difference time integration scheme. Eng Comput (swansea, Wales) 21:278–303. https://doi.org/10.1108/02644400410519794

RAC (2023) Pothole Index—statistics and data for UK roads. https://www.rac.co.uk/drive/advice/driving-advice/rac-pothole-index-statistics-data-and-projections/. Accessed 12 Sept 2023

Rackl M, Hanley KJ (2017) A methodical calibration procedure for discrete element models. Powder Technol 307:73–83. https://doi.org/10.1016/j.powtec.2016.11.048

Salemi M, Wang H (2018) Image-aided random aggregate packing for computational modeling of asphalt concrete microstructure. Constr Build Mater 177:467–476. https://doi.org/10.1016/j.conbuildmat.2018.05.139

Tang X, Paluszny A, Zimmerman RW (2013) Energy conservative property of impulse-based methods for collision resolution. Int J Numer Methods Eng 95:529–540. https://doi.org/10.1002/nme.4537

Tuvayanond W, Prasittisopin L (2023) Design for manufacture and assembly of digital fabrication and additive manufacturing in construction: a review. Buildings 13:429. https://doi.org/10.3390/buildings13020429

Velocity, Spray Injection Patching (2023) https://velocityroads.co.uk/spray-injection-patching/. Accessed 12 Sept 2023

Wang T, Dra YASS, Cai X, Cheng Z, Zhang D, Lin Y, Yu H (2022) Advanced cold patching materials (CPMs) for asphalt pavement pothole rehabilitation: state of the art. J Clean Prod 366:133001. https://doi.org/10.1016/j.jclepro.2022.133001

Xiao B, Chen C, Yin X (2022) Recent advancements of robotics in construction. Autom Constr 144:104591. https://doi.org/10.1016/j.autcon.2022.104591

Yao H, Xu M, Liu J, Liu Y, Ji J, You Z (2022) Literature review on the discrete element method in asphalt mixtures. Front Mater 9:879245. https://doi.org/10.3389/fmats.2022.879245

Zhang P, Cheng YC, Tao JL, Jiao YB (2016) Molding process design for asphalt mixture based on response surface methodology. J Mater Civ Eng 28:04016120. https://doi.org/10.1061/(asce)mt.1943-5533.0001640